2019 IEEE-RAS 19th International Conference on Humanoid Robots (Humanoids)
Toronto, Canada. October 15-17, 2019

Exoskeleton Arm Pronation/Supination Assistance Mechanism With A Guided Double Rod System

Miha Dežman[1,2], Tamim Asfour[3], Aleš Ude[1] and Andrej Gams[1]

***Abstract*— The wrist pronation and supination movement is important in everyday manipulation tasks. Users with limitations in this particular movement have severe impairment. While advanced upper-arm exoskeletons can assist in the pronation/supination movement, typically, the resulting exoskeleton frame that combines both the elbow joint and pronation/supination mechanism becomes heavy and bulky with a large volume. We propose a new arm pronation supination mechanism that is integrated into the exoskeleton frame and has a reduced weight and volume penalty. The mechanism functions via a double rod system, where the rods are guided through a set of specially shaped grooves that finally result in the rotation of the wrist component. The paper presents a plastic rapid prototype built using 3D additive technologies. The mechanism is actuated via a Bowden cable transmission. Its underlying kinematics are experimentally evaluated using an external motion capture system to identify its advantages and disadvantages.**

I. INTRODUCTION

Among the different human upper-limb joints, wrist pronation and supination is one of the movements that enables the human arm dexterity and performance at various tasks. Limitation of this movement creates a major impairment for patients during their daily life activities [1]. Exoskeleton wearable robots intended for the upper-limb assistance, as presented in, for example, [2], [3], assist also in the forearm pronation and supination.

Biologically, the elbow joint is a combination of a hinge joint and a pivot joint [4]. Therefore, the exoskeleton frame has to allow for and comply with the elbow flexion/extension movement as well as with the pronation and supination assistance. The combination of flexion/extension and pronation/supination is not easy to realize in the exoskeleton frame. Most often, the pronation and supination rotation of the exoskeleton frame is enabled via a circular bearing located somewhere in-between the elbow and the wrist [5], [6]. This bearing can be either only C-shaped, or a full ring. The difference is that in the full ring case, the user has to put his arm through the bearing ring when donning the exoskeleton. The bearing diameter needs to be large enough for the palm to pass through. On the other side, a C-shaped bearing allows the user to put his arm through the opening from the side, easing the exoskeleton donning and somewhat reducing the bearing diameter. However, the C-shaped version might not allow for a full-continuous rotation.

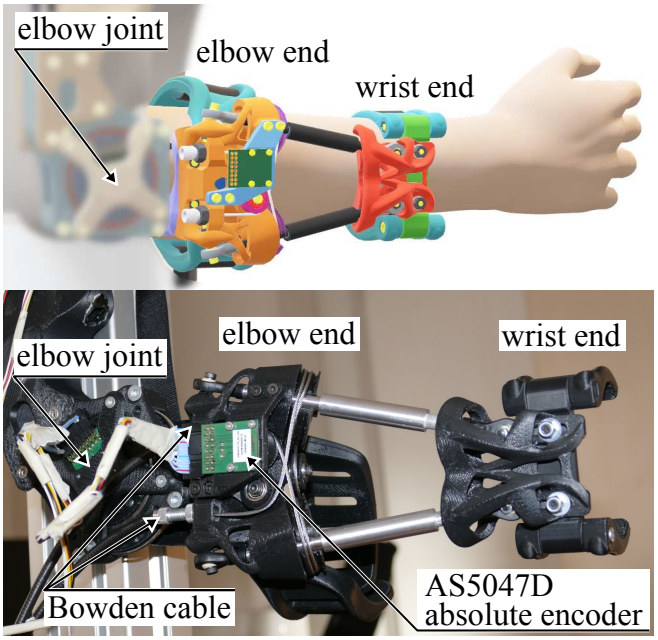

Fig. 1. Lower-arm pronation/supination assistance exoskeleton model.

Such a ring bearing mechanism can be actuated via a direct gear, since the ring diameter is large and achieves a relatively big transmission ratio in combination with a smaller gear [7]. In contrast to the classical bearing design approaches, the Harmony exoskeleton [8] presents a complementary solution. Their mechanism is built on the side of the lower arm in a compact form and allows for an external rotation, however that requires a lot of space outwards, away from the lower-arm.

Many times the lower arm frame is expanded onto the user's wrist joint [9], [10]. One way to assist at the human wrist joint is through a parallel actuated mechanism [11], [12]. Use of pneumatic actuators offers another way for actuation with the additional advantage of mechanical compliance [13]. Meanwhile, the bearing ring bears the full load of the subsequent components and despite being a very rigid solution, it requires a large volume and results in a bulky and heavy exoskeleton lower arm frame.

Assuming that the arm exoskeleton is fixed or grounded at the shoulder, a lot of the weight is thus concentrated at the lower arm area that is far from the shoulder joint. Such an exoskeleton has a decreased dynamic performance due to a higher inertia. A lighter robotic frame allows for a more dynamic movement, reduces the energy consumption and

[1]Department of Automation, Biocybernetics and Robotics, Jozef Stefan Institute, Jamova cesta 39, 1000 Ljubljana, Slovenia,
(Miha Dežman, miha.dezman@ijs.si)
[2]Jozef Stefan International Postgraduate School, Jamova 39, 1000 Ljubljana, Slovenia,
[3]High Performance Humanoid Technologies (H^2T), Institute for Anthropomatics and Robotics (IAR), Karlsruhe Institute of Technology (KIT), Adenauerring 2, 76131 Karlsruhe, Germany.

increases the intrinsic safety [14].

The motors take up a big portion of the devices weight. Relocating the motors away from the exoskeleton's joints via a power transmission can reduce the frame weight. Such exoskeletons typically employ a Bowden cable transmission [15]. Most devices in a rehabilitation scenario are stationary and the user movements are relatively slow. Here the increased weight is not as problematic. However, a fully portable exoskeleton version benefits from having a minimal weight, not only to increase safety, but also to increase its energy efficiency. A lower inertia also results in a more transparent user experience.

This work proposes and kinematically evaluates a new arm pronation-supination rotation degree of freedom for an exoskeleton. A rendered image of the device and the built prototype are presented in Fig. 1. The main benefit of the proposed design are the two guided rods that replace the traditional ring bearing to reduce the overall volume requirements and weight. The proposed implementation is actuated via a Bowden cable transmission. As an alternative, a motor could also be integrated to directly drive the two rods using gears. A prototype was built to test the feasibility of the proposed experimental design and evaluate its ability to rotate.

The manuscript is organized as follows: The new pronation/supination mechanism is presented and explained in Section II. Next, in Section III, a mathematical model is constructed to calculate the necessary rotation paths and groove shapes. Section IV presents the prototype and the experimental evaluation of the mechanism's kinematics. The results are analyzed and discussed in Section V, followed by a conclusion.

II. Pronation Supination Mechanism

The mechanism is split into the wrist-end and elbow-end, as seen in Fig. 2. The wrist-end is attached just behind the user's wrist as seen in Fig. 1. The physical interface

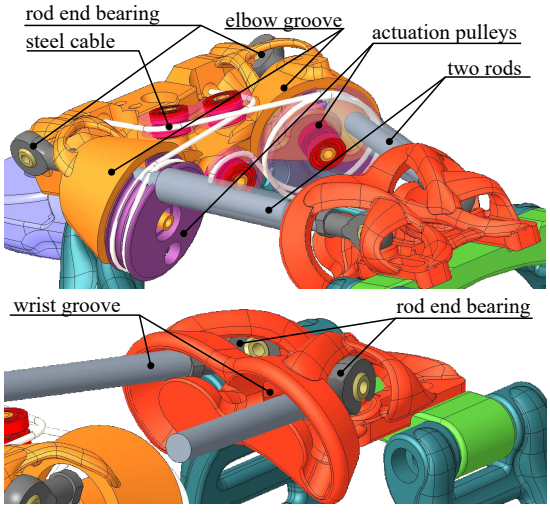

Fig. 2. The components relevant to the mechanism's actuation: elbow-end (top) and wrist-end (bottom).

currently uses partially rigid straps for attachment onto a user's arm. Mechanism rotates the wrist-end component and thereby transmits the force to user's hand. The quality of the partially rigid straps attachment will be evaluated at a later date, as the present work evaluates only the rotation of the pronation-supination mechanism. The elbow-end is attached to the rest of the exoskeleton and does not rotate. It partially supports the user's forearm just in front of the elbow joint using its attachment strap.

The wrist and elbow ends are connected via two rods that can contract or extend for linear translation. The linear translation of the rods is passive and not directly actuated. The rods are connected at the elbow-end component via their respective plastic rod end-bearing. Another pair of plastic rod end-bearings is used at the wrist-end. Fig. 2 shows more details. Any friction in the linear rods movement does not prevent the rotation of the end wrist, however, the friction is large enough to make the mechanism non-backdrivable. The mechanism stays stable, because the two rods are positioned at an angle relative to each other.

Fig. 3 shows the rotation of the mechanism. Observe that

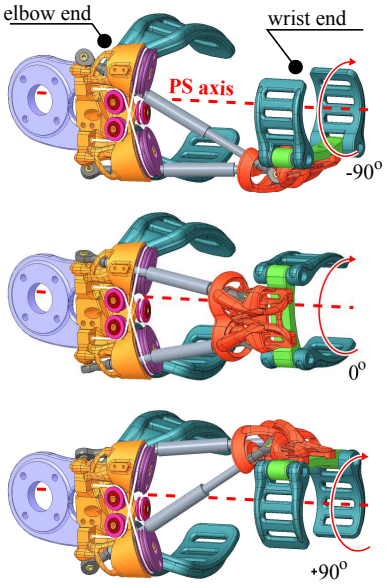

Fig. 3. A 3D model of the lower-arm pronation-supination mechanism while rotating from -90^o through 0^o to 90^o around the pronation/supination axis (PS axis).

the two rod system changes in its length during the rotation. In Fig. 2, behind the transparent actuation pulley, observe the grooves that guide the rods. Both rods are actuated via the two pulleys. This is possible because the rods rotate in a conical shape. Tracing a point on the respective rod results in a quasi-circle trajectory. The quasi-circle is used to find a center of rotation and exploited for the actuation pulley axis placement. The center is approximated and located via three points.

The rods are attached to the pulley with some compliance in the radial direction for the compensation of any conical shape imperfections. Both pulleys are actuated via a cable,

which is routed around them and comes out at the elbow-end component. The elbow and the wrist components both contain guiding grooves, which results in one free degree-of-freedom of the whole mechanism. Additional smaller pulleys are added to guide the cable through the elbow-end component.

III. Mathematical Model

The mathematical model describes the rotation of various points around a fixed axis and involves some distance calculations in order to trace the shape of the guiding grooves. It is assumed that the human lowerarm or pronation/supination axis is fixed to simplify the design at this stage. In reality, the lowerarm axis center-of-rotation moves during pronation and supination [17]–[19]. However, determining the exact position of the rotation axis through the whole pronation-supination movement range is difficult [17]–[19] and goes beyond the scope of our research. The rotation limit of the forearm pronation and supination is approximated to be $\pm 90^o$ [20].

Fig. 4 gathers the relevant parameters. The points

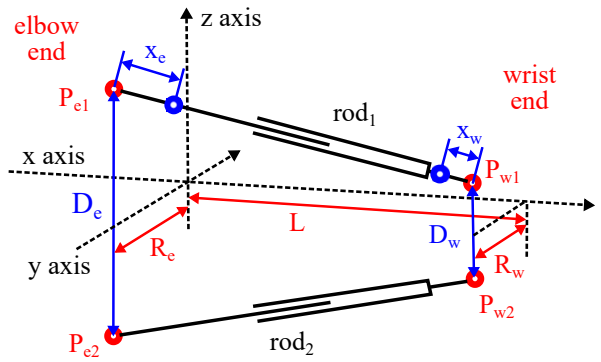

Fig. 4. A simplified representation of the important parameters of the mathematical model.

$P_{e1}, P_{e2}, P_{w1}, P_{w2}$ represent the connection points for the two rods. At those points, the two rods are connected to either the elbow-end exoskeleton frame component or the wrist-end through plastic rod end-bearings. To calculate the shape of the elbow-end grooves, the wrist-end, i.e., the points P_{w1}, P_{w2} are rotated around the mechanism's axis. For convenience, the mechanism's axis is placed on the x axis of the global coordinate system.

Parameter L presents the distance between the elbow-end and the wrist-end, projected onto the global x axis. Parameters x_e and x_w represent the distance of the tracing points

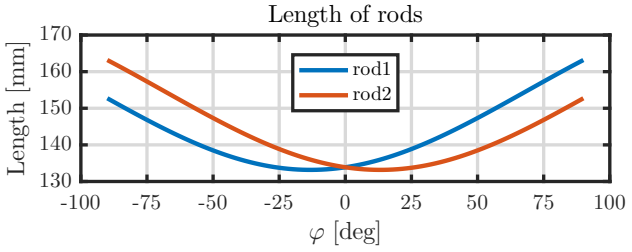

Fig. 5. The length of "rod1" and "rod2" during the rotation.

from their respective pivots and are selected empirically to trace the curves at the desired distance. The length of the two rods changes, as can be seen in Fig. 5.

The lengths D_e and D_w represent the distance between the rod-end bearings and indirectly the lateral size of the mechanism. The larger the two lengths, the wider the mechanism. The lengths R_e and R_w represent the radius to the mechanism's axis and indirectly represent the diameter of the user's lower-arm.

The mathematical model parameters are gathered in Table I. The coordinates of the mechanism pivot points are

TABLE I
MATHEMATICAL MODEL PARAMETERS

Parameter	Value	Parameter	Value
D_e	80 [mm]	D_w	30 [mm]
R_e	65 [mm]	R_w	45 [mm]
L	130 [mm]	φ	-90 - 90 [^{o}]

calculated as:

$$P_{e1} = \left[0, -R_e, \frac{D_e}{2}\right], \quad (1) \quad P_{w1} = \left[L, -R_w, \frac{D_w}{2}\right], \quad (2)$$

$$P_{e2} = \left[0, -R_e, -\frac{D_e}{2}\right], \quad (3) \quad P_{w2} = \left[L, -R_w, -\frac{D_w}{2}\right]. \quad (4)$$

A. Elbow-end guiding grooves

To calculate shape of the elbow groove, the elbow-end is fixed. The wrist-end points can be rotated using rotation matrix transformation [21, p. 13]:

$$W_{Pw1}(\varphi) = P_{w1} \begin{bmatrix} 1 & 0 & 0 \\ 0 & \cos(\varphi) & -\sin(\varphi) \\ 0 & \sin(\varphi) & \cos(\varphi) \end{bmatrix}. \quad (5)$$

The points P_{e1} and W_{Pw1} are used to calculate the length of rod1 ($L_{erod1}(\varphi)$) as it rotates for φ:

$$L_{erod1}(\varphi) = \sqrt{(P_{e1} - W_{Pw1}(\varphi))(P_{e1} - W_{Pw1}(\varphi))'}. \quad (6)$$

Next, a point is placed on rod1 at a distance (x_e) from the elbow-end pivot point. A relative distance factor $\delta_{e1}(x_e, \varphi)$ is defined as:

$$\delta_{e1}(x_e, \varphi) = x_e / L_{erod1}(\varphi), \quad (7)$$

where $\delta_{e1}(x_e, \varphi)$ is related to the desired distance x_e and the rotation of the wrist-end component φ.

Finally, the point at the relative distance $\delta_{e1}(x_e, \varphi)$ can be traced:

$$T_{e1}(x_e, \varphi) = P_{e1} + (W_{Pw1}(\varphi) - P_{e1})\delta_{e1}(x_e, \varphi). \quad (8)$$

B. Wrist-end guiding grooves

To calculate the wrist-end guiding grooves, the same procedure can be used as for the wrist-end, however, this time the wrist-end is fixed and the elbow-end is rotated.

$$W_{Pe1}(\varphi) = P_{e1} \begin{bmatrix} 1 & 0 & 0 \\ 0 & \cos(\varphi) & -\sin(\varphi) \\ 0 & \sin(\varphi) & \cos(\varphi) \end{bmatrix}. \quad (9)$$

The points P_{w1} and W_{Pe1} are again used used to calculate the length of the rods. To trace the trajectories of the guiding groove, a point can be placed a distance (x_w) away from the respective pivot point on the wrist-end.

The $L_{wrod1}(\varphi)$ is the rod length as it rotates for φ, and is calculated using the following equation:

$$L_{wrod1}(\varphi) = \sqrt{(P_{w1} - W_{Pe1}(\varphi))(P_{w1} - W_{Pe1}(\varphi))'}. \quad (10)$$

The coordinates at a specific distance can be found using:

$$\delta_w(x_w, \varphi) = x_w / L_{wrod1}(\varphi), \quad (11)$$

where $\delta_w(x_w, \varphi)$ is a distance factor related to the desired distance x_w and the rotation φ of the elbow component. Finally, the point can be traced to calculate the trajectory:

$$T_{w1}(x_w, \varphi) = P_{w1} + (W_{Pe1}(\varphi) - P_{w1})\delta_w(x_w, \varphi). \quad (12)$$

IV. The Prototype and the Experiment

The elbow-end is created using eq. (8). This creates the curves $T_{e1}(x_e = 20, \varphi = \text{-}90^o - 90^o)$ and $T_{e1}(x_e = 48, \varphi = \text{-}90^o - 90^o)$. The wrist-end is created using eq. (12). The result are the curves $T_{e1}(x_w = 10, \varphi = \text{-}90^o - 90^o)$ and $T_{e1}(x_w = 30, \varphi = \text{-}90^o - 90^o)$. These trajectories can be mirrored along the $x - y$ plane to create the bottom curves, as seen in Fig. 6. Their negative equivalents can be traced by flipping their z coordinates. The equations for the bottom

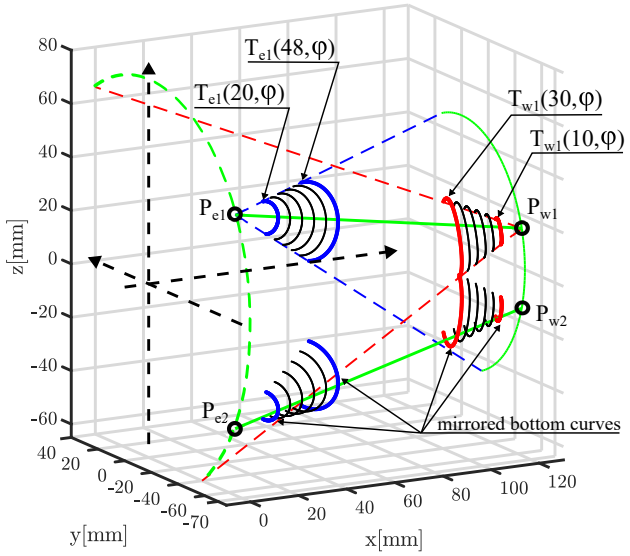

Fig. 6. The elbow-end guiding groove trajectory in blue color and the wrist-end guiding grooves in red color. The green line represents the two rods. The blue/red dashed lines represents the position of the two rods at the minimum and maximum rotation.

curves are therefore not written as they are mirrored in a CAD software. Both the upper curves and the bottom mirrored curves are shown in Fig. 6. In the CAD software, the curves can be generated using the above equations and then used to create the sliding surfaces. Fig. 7 represents a simplified model of the resulting elbow-end and wrist-end.

Several strengthening features were later added/modelled on top of both parts to increase their rigidity. The final

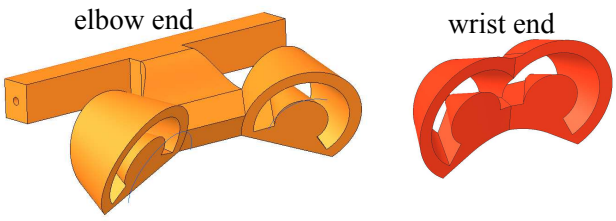

Fig. 7. The initial CAD model of the guiding grooves on the elbow-end and the wrist-end.

prototype can be seen in Fig. 1. The parts were manufactured out of ABS plastic material using the 3D additive technologies. The mechanical complexity of the plastic parts is high, however, the parts can be further simplified and later manufactured via more traditional technologies. The current prototype serves mostly to investigate the feasibility of the proposed mechanism, therefore, it does not need to be very durable. The rods connecting both frame parts were manufactured out of aluminium. IGUS Igubal® rod-end bearings are used to connect the rods to the elbow and the wrist-end part. An AS5047D encoder was integrated into the frame, as shown in Fig. 1, to be later used for angle measurement.

At this stage, only the mechanism's kinematic properties are investigated. The goal of the experiment is to measure the actual rotation of the wrist-end component and compare it to the predicted rotation.

Optotrak motion capture system was used to measure the position of the six markers placed on the mechanism. They were arranged in 2 triangle configurations. All markers can be seen in Fig. 8. Markers numbered 1, 2 and 3 were mounted onto the rotating element, such that the mechanism's rotation axis was approximately at the center of the marker triangle. Markers 4, 5 and 6 were mounted on the base of the mechanism and were used to monitor the movement of the mechanism's base. The system was actuated via a Bowden cable transmission. At this stage,

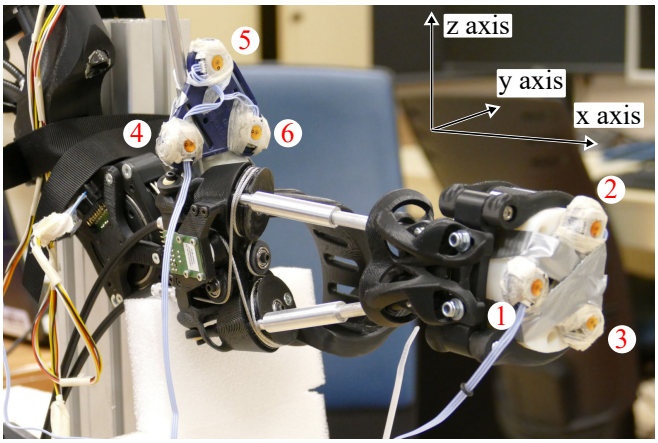

Fig. 8. The experimental setup consisting of the mechanism prototype and Optotrak active markers. The markers are numbered. The Optotrak coordinate system is shown in the top right corner and oriented to be the same as in the mathematical model and in the CAD model.

feedforward position control is used to move the mechanism in both directions. The movement started at 0 deg → -80 deg → 0 deg → 80 deg → 0 deg. Due to the inaccuracies of the plastic components and slack of the cable, the movement was limited to approximately ±80 deg instead of the initial ±90 deg. The motor's actual rotation is measured at the motor shaft using a relative encoder. The motion of the markers was measured and compared to the desired, commanded behaviour.

V. Analysis of the Results and Discussion

The Optotrak system outputs the position coordinates of each marker. Let $M_{\mathrm{j}}(t)$ represents the time dependent coordinate vector that describes the coordinates of marker j at time t.

$$M_{\mathrm{j}}(t) = [x_{\mathrm{j}}(t), y_{\mathrm{j}}(t), z_{\mathrm{j}}(t)]\,; \text{ where: } \mathrm{j} \in [\ \mathrm{c},\ 1,\ 2,\ 3,\ 4,\ 5,\ 6\ ]\,. \tag{13}$$

The $M_{\mathrm{j}}(t)$ gathers the trajectory in relation to time, however, the t is henceforth not written. Via the calculation of the equilateral triangle center formed by markers 1, 2 and 3, the mechanism's axis is approximated with its centroid:

$$M_{\mathrm{c}} = \frac{M_1 + M_2 + M_3}{3}, \tag{14}$$

where M_{c} is the centroid of the marker (M_1, M_2, M_3) triangle.

All the marker measurements are shown in Fig. 9.

It can be observed that the mechanism does rotate around its axis when actuated through the pulleys. However, a lot of position fluctuations are observed. Observe that the red axis approximation fluctuates for ±7 mm in the z and y axis directions. The primary cause for these displacements are the tolerances and deformations of the plastic components. Some error can also be attributed to the slack and stretching of the Bowden cable. The cables were only lightly tensioned to minimize the deformations and to stay in the acceptable load levels of the plastic components. Higher tension in the cable would improve the quality of the results in a more rigid system.

The top view shows the axial movement of the mechanism. This happens because both actuation pulley's do not move in phase. Since the system is not properly tensioned, due to the reasons described above, there is some slack in the cable that connects both pulleys. There are several smaller pulleys that guide the cable. Their low-diameter results in an increased slack due to the cable bending moment. This slack causes the actuation pulleys to be out of phase. The phase differences result in a larger distance between both rods, which is again permitted due to the limited tolerances of the plastic components.

One way to overcome this limitation would be to upgrade the actuation pulleys (see the pulleys in Fig. 2) with three bewel gears to lock the rotation between them. This can be realized in the next design iteration.

It is assumed that the markers 1,2 and 3 lie on the $y-z$ plane. The centroid coordinates can be used to move the rotation center of the marker triangle, i.e., the mechanism rotation axis, to the origin of the $y-z$ axis plane. Thus we can show the relative displacement of markers against the centroid center. This is realized using the following equation:

$$M_{\mathrm{ic}} = M_{\mathrm{i}} - M_{\mathrm{c}}; \quad \text{where:} \quad i \in [\ 1,\ 2,\ 3]\,. \tag{15}$$

M_{ic} are the vectors of different markers centered to the origin.

The new markers $(M_{1\mathrm{c}}, M_{2\mathrm{c}}, M_{3\mathrm{c}}, M_{\mathrm{c}})$ can be seen in Fig. 10(left). As can be seen, the marker triangle rotation results in three approximately coaxial circles. Since the marker circles are nearly coaxial, the y and z marker coordinates are used to directly calculate the rotation angle of the mechanism. Thus, we avoid the coordinate system transformations, which would not notably improve our angle

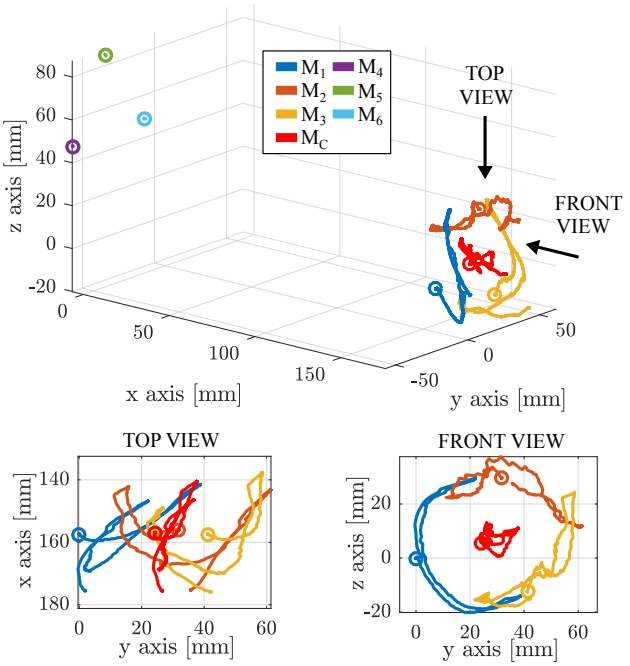

Fig. 9. The marker position data. The system has the same configuration as shown in Fig. 8. Two additional views (top, front) are shown for better data readability. The red line represents the centroid. The small circles represent the start of the movement.

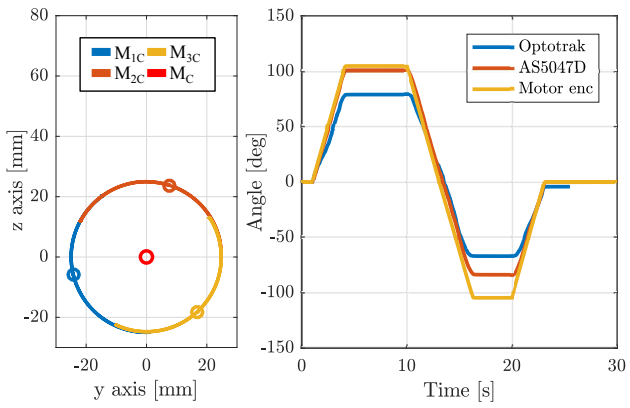

Fig. 10. The center transformed marker trajectories are shown in *left* graph. The *right* graph shows the comparison of the angle calculated from Optotrak measurements, the AS5047D encoder and the encoder placed at the motor shaft (with transmission).

calculation. The angles are calculated using arctan for each coordinate of the marker trajectory. Note that in order to operate in the area of small angles, each point is rotated by the angle of its predecessor to calculate the angle difference. The final angle is calculated using the cumulated angle differences.

In Fig. 10(right), 3 different angle measurements are shown. The measurement of the encoder positioned at the motor represents the commanded rotation input. The Optotrak angle measurement shows the actual rotation of the mechanism. Lastly, the AS5047D encoder serves as a means to measure the absolute angle. The Fig. 10(right) shows the quality comparison of its measurement against the other two. As stated before, it is clear that there is a lot of stretching of the cable, because the individual angle measurements do not coincide nicely. However, their shapes show improvement possibilities using calibration methods. The AS5047D can ascertain the absolute angle of the mechanism, however, it might not be of sufficient quality as a feedback signal to control motors.

Overall, the mechanism is sturdy in lateral direction and can carry weight. However, one of the current flaws is that the mechanism carries a limited load along the rotation axis. This flaw can be improved with the phase locking of the actuation pulleys.

VI. CONCLUSIONS

The proposed mechanism rotates around its own axis when it is actuated with the actuation pulleys. While the performance is limited, at this stage, it can be attributed to the lower quality of plastic components. Cable stretching and cable slack are present because the Bowden cable is not tensioned properly. The primary reason lies in the quality and a limited strength of the plastic components, which originate from the rapid prototyping. While several mechanism aspects still need to be investigated, the current results support further research development of the proposed mechanism.

In the future, the dynamic performance of the mechanism and its torque transfer characteristics will be evaluated. Currently, the actual user were not yet included in the design iterations, but need to be considered in the future.

ACKNOWLEDGMENT

The projects was supported by the following institutions: German Academic Exchange Service (DAAD), for financing a short research stay at Karlsruhe Institute of Technology. The Slovenian Research Agency (ARRS), research core funding No. PR-06812. The authors would like to thank team members of High Performance Humanoid Technologies (H^2T) laboratory at KIT for their support.

REFERENCES

[1] "Dealing with problems of pro- and supination of the lower arm." https://www.bighandevent.com/session/dealing-with-problems-of-pro-and-supination-of-the-lower-arm/. Accessed: 2019-06-30.

[2] H. S. Lo and S. Q. Xie, "Exoskeleton robots for upper-limb rehabilitation state of the art and future prospects," *Medical Engineering and Physics*, vol. 34, no. 3, pp. 261 – 268, 2012.

[3] R. Gopura, D. Bandara, K. Kiguchi, and G. Mann, "Developments in hardware systems of active upper-limb exoskeleton robots: A review," *Robotics and Autonomous Systems*, vol. 75, pp. 203 – 220, 2016.

[4] J. Hamill and K. M. Knutzen, *Biomechanical basis of human movement*. Lippincott Williams & Wilkins, 2006.

[5] K. Kiguchi, R. Esaki, T. Tsuruta, K. Watanabe, and T. Fukuda, "An exoskeleton for human elbow and forearm motion assist," in *Proceedings 2003 IEEE/RSJ International Conference on Intelligent Robots and Systems (IROS 2003)(Cat. No. 03CH37453)*, vol. 4, pp. 3600–3605, IEEE, 2003.

[6] R. A. R. C. Gopura and K. Kiguchi, "An exoskeleton robot for human forearm and wrist motion assist," *Journal of Advanced Mechanical Design, Systems, and Manufacturing*, vol. 2, no. 6, pp. 1067–1083, 2008.

[7] M. Rahman, M. Saad, J. Kenné, and P. Archambault, "Exoskeleton robot for rehabilitation of elbow and forearm movements," in *18th Mediterranean Conference on Control and Automation, MED'10*, pp. 1567–1572, IEEE, 2010.

[8] B. Kim and A. D. Deshpande, "An upper-body rehabilitation exoskeleton harmony with an anatomical shoulder mechanism: Design, modeling, control, and performance evaluation," *The International Journal of Robotics Research*, vol. 36, no. 4, pp. 414–435, 2017.

[9] J. A. Martinez, P. Ng, S. Lu, M. S. Campagna, and O. Celik, "Design of wrist gimbal: A forearm and wrist exoskeleton for stroke rehabilitation," in *2013 IEEE 13th International Conference on Rehabilitation Robotics (ICORR)*, pp. 1–6, IEEE, 2013.

[10] D. Buongiorno, E. Sotgiu, D. Leonardis, S. Marcheschi, M. Solazzi, and A. Frisoli, "Wres: a novel 3 dof wrist exoskeleton with tendon-driven differential transmission for neuro-rehabilitation and teleoperation," *IEEE Robotics and Automation Letters*, vol. 3, no. 3, pp. 2152–2159, 2018.

[11] A. Gupta, M. K. O'Malley, V. Patoglu, and C. Burgar, "Design, control and performance of ricewrist: a force feedback wrist exoskeleton for rehabilitation and training," *The International Journal of Robotics Research*, vol. 27, no. 2, pp. 233–251, 2008.

[12] A. U. Pehlivan, O. Celik, and M. K. O'Malley, "Mechanical design of a distal arm exoskeleton for stroke and spinal cord injury rehabilitation," in *2011 IEEE International Conference on Rehabilitation Robotics*, pp. 1–5, IEEE, 2011.

[13] J. Huang, X. Tu, and J. He, "Design and evaluation of the rupert wearable upper extremity exoskeleton robot for clinical and in-home therapies," *IEEE transactions on systems, man, and cybernetics: systems*, vol. 46, no. 7, pp. 926–935, 2015.

[14] A. Albu-Schäffer, O. Eiberger, *et al.*, "Soft robotics," *IEEE Robotics & Automation Magazine*, vol. 15, no. 3, pp. 20–30, 2008.

[15] K. Kiguchi, R. Esaki, and T. Fukuda, "Development of a wearable exoskeleton for daily forearm motion assist," *Advanced Robotics*, vol. 19, no. 7, pp. 751–771, 2005.

[16] E. Rocon, J. Belda-Lois, A. Ruiz, M. Manto, J. C. Moreno, and J. Pons, "Design and validation of a rehabilitation robotic exoskeleton for tremor assessment and suppression," *IEEE Transactions on Neural Systems and Rehabilitation Engineering*, vol. 15, no. 3, pp. 367–378, 2007.

[17] K. O. Matsuki, K. Matsuki, S. Mu, T. Sasho, K. Nakagawa, N. Ochiai, K. Takahashi, and S. A. Banks, "In vivo 3d kinematics of normal forearms: Analysis of dynamic forearm rotation," *Clinical Biomechanics*, vol. 25, no. 10, pp. 979 – 983, 2010.

[18] T. Nakamura, Y. Yabe, Y. Horiuchi, and N. Yamazaki, "In vivo motion analysis of forearm rotation utilizing magnetic resonance imaging," *Clinical Biomechanics*, vol. 14, no. 5, pp. 315 – 320, 1999.

[19] S. C. Tay, R. van Riet, T. Kazunari, K. K. Amrami, K.-N. An, and R. A. Berger, "In-vivo kinematic analysis of forearm rotation using helical axis analysis," *Clinical Biomechanics*, vol. 25, no. 7, pp. 655 – 659, 2010.

[20] A. Gupta and M. K. O'Malley, "Robotic exoskeletons for upper extremity rehabilitation," *Rehabilitation Robotics*, vol. 10, p. 5171, 2007.

[21] B. Siciliano and O. Khatib, *Springer Handbook of Robotics*. Berlin, Heidelberg: Springer-Verlag, 2016.